JOURNAL OF MATERIALS SCIENCE **39** (2004) 5925–5937

Processing, properties and arc jet oxidation of hafnium diboride/silicon carbide ultra high temperature ceramics

M. GASCH
ELORET Corporation, 690 W. Fremont Ave., Sunnyvale, CA 94087, USA
D. ELLERBY, E. IRBY, S. BECKMAN
NASA, Ames Research Center, MS 234-1, Moffett Field, CA 94035, USA
M. GUSMAN
ELORET Corporation, 690 W. Fremont Ave., Sunnyvale, CA 94087, USA
S. JOHNSON
NASA, Ames Research Center, MS 234-1, Moffett Field, CA 94035, USA
E-mail: Sylvia.M.Johnson@nasa.gov

The processing and properties of HfB_2-20 vol%SiC ultra high temperature ceramics were examined. Dense billets were fabricated by hot-pressing raw powders in a graphite element furnace for 1 h at 2200°C. Specimens were then tested for hardness, mechanical strength, thermal properties and oxidation resistance in a simulated re-entry environment. Thermal conductivity of the current materials was found to be less than previous work had determined while the strength was greater. Oxidation testing of two flat-face models was conducted, at two conditions, for two 10-min durations each. It was concluded that passive oxidation of SiC plays a role in determining the steady-state surface temperatures below 1700°C. Above 1700°C, temperatures are controlled by the properties of a thick HfO_2 layer and active oxidation of the SiC phase. *© 2004 Kluwer Academic Publishers*

1. Introduction

Ceramic borides, such as hafnium diboride (HfB_2) and zirconium diboride (ZrB_2), are members of a family of materials with extremely high melting temperatures which have been referred to as Ultra High Temperature Ceramics (UHTCs). UHTCs constitute a class of promising materials for use in high temperature applications, such as sharp leading edges on future generations of reentry vehicles, because of their high melting points and relatively good oxidation resistance in reentry environments [1].

Because of the extremely high melting temperatures of these diboride materials (i.e., melting temperature of HfB_2 is ∼3300°C as shown in Fig. 1) hot pressing at temperatures >2000°C and at high pressures is required to produce dense materials. The most extensive collection of work conducted on diborides of Hf and Zr was performed by ManLabs in the 1960's and 70's under contract with the Air Force. Some of the early work by ManLabs used very high pressure (1–2 GPa) hot pressing to densify the pure diborides [1].

In addition to the pure diborides, ManLabs investigated the influence of a variety of additives, including C and SiC, on the processing, oxidation resistance and thermal shock resistance of Hf and Zr diborides [2]. Their work, in both static furnace experiments and arc jet testing, showed that the addition of SiC improved the oxidation resistance of Hf and Zr diborides. SiC additions ranging from 5–50 vol% were studied. The work indicated that 20 vol% of a SiC particulate additive resulted in the optimum oxidation resistance [3]. The SiC additions were also found to improve the processing of the materials by reducing the maximum temperature and pressure required to densify the materials and by reducing grain growth of the diboride phase [3].

A number of other studies have been conducted on the oxidation resistance of Hf and Zr diboride materials of various compositions, but these have focused primarily on static or flowing air studies under ambient pressure, and few studies have evaluated their oxidation behavior in simulated reentry environments [4–10]. Static or flowing air oxidation studies under ambient conditions may not provide an accurate representation of a material's behavior in the unique environment encountered during re-entry. In addition, the relative oxidation resistance of two materials measured in a typical furnace oxidation study may not pertain when testing the same two materials in a reentry environment. Arc jet facilities, on the other hand, provide sustained conditions that are similar to the aerothermal environment experienced during reentry. The testing results are used to understand the thermal performance of materials and systems under controlled aerothermal heating conditions. Arc jet testing is also used to validate

0022–2461 © *2004 Kluwer Academic Publishers*

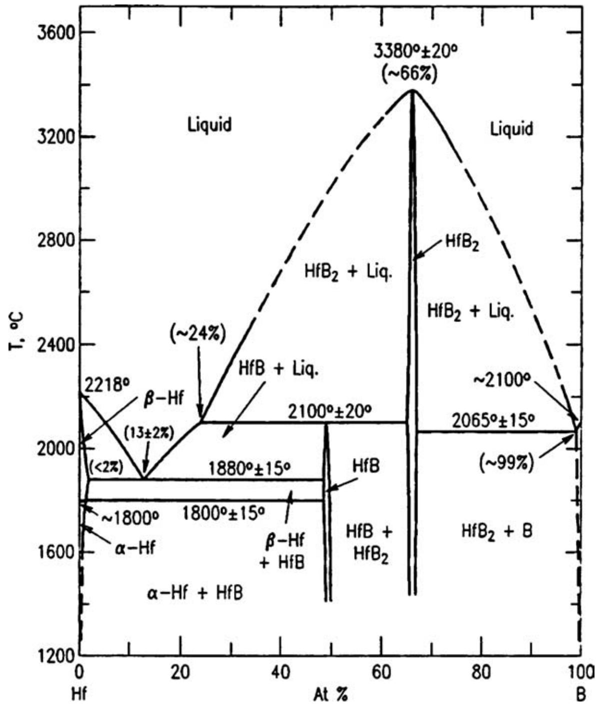

Figure 1 Hafnium diboride phase diagram.

the numerical models of materials and systems that are used as design tools [11]. Arc jet testing provides the best ground-based simulation of the reentry environment. Nevertheless, there are a number of differences between the arc jet environment and the reentry environment that must be accounted for when designing an arc jet experiment, and when interpreting the data. For example, surface catalycity can play a more significant role during arc jet testing than it does in flight, because a higher proportion of the air molecules are dissociated in the arc jet environment.

NASA Ames began work on UHTCs in the early 1990's. In 1997 and 2000 Ames demonstrated the use of UHTC sharp leading edges on the Sharp Hypersonic Aero-thermodynamic Research Probe-Ballistic experiments 1 and 2 (SHARP-B1 and SHARP-B2) [12]. The SHARP-B1 vehicle tested a HfB_2-20 vol%SiC nose tip with a 3.5 mm radius. The SHARP-B2 vehicle tested three different leading edge materials, HfB_2-SiC, ZrB_2-SiC and ZrB_2-SiC-C.

For the sharp wing leading edge applications envisioned for these materials on future reentry vehicles, in addition to oxidation resistance, high thermal conductivity is desirable. In the family of UHTCs, the diborides typically have the highest conductivities. High conductivity improves a material's thermal shock resistance by reducing temperature gradients and thermal stresses in the material. A higher conductivity also allows more energy to be conducted away from the stagnation point on the wing leading edge. That energy is subsequently reradiated away from lower temperature regions, along the outer surface of the wing leading edge component. This process may enable the vehicle to operate under higher heat flux conditions, improving its performance.

The current study has investigated a method of processing HfB_2-20 vol% SiC particulate composites, using conventional hot pressing. Mechanical and thermal properties of the materials have been evaluated and compared to the results from heritage materials of similar compositions (SHARP-B2). Finally, a preliminary investigation of the oxidation behavior of this composition in a simulated reentry environment was begun and testing was conducted at NASA Ames Research Center (ARC) in the Interactive Heating Facility (IHF).

2. Experimental procedure

The raw powders used in this work were −325 mesh HfB_2 from Cerac Inc. and 1–2 μm SiC from H.C. Starck Inc. Analysis of the impurities present in the materials was conducted by NSL Analytical Services (Cleveland, OH). Samples were analyzed, using direct current plasma emission spectroscopy to determine metallic impurities, and using inert gas fusion to determine oxygen and carbon impurities. Analysis of the crystalline phases present in the raw and mixed powders was performed with X-ray Diffraction (Scintag X-ray diffractometer) using Cu K_α radiation. Particle size of the raw and milled powders was measured using laser light scattering (Malvern). Light scattering patterns were analyzed with computer software that used the Mie theory. Prior to hot pressing, the HfB_2-20 vol% SiC raw powders were wet-milled with WC milling media in either a planetary mill (Fritsch) or an attrition mill (Union Carbide). The milled powders were carefully dried to prevent phase segregation between the HfB_2 ($\rho = 11.12$ g/cc) and the SiC ($\rho = 3.2$ g/cc). After drying, the powders were loaded into either 25 or 50 mm diameter graphite dies, lined with graphfoil. Hot pressing cycles were initiated in a graphite element resistance furnace (Thermal Technologies) with vacuum levels of <200 milliTorr. Above 1600°C, the partial pressure of carbon in the furnace increased significantly and degraded the vacuum. Consequently the furnace was back-filled with one atmosphere of inert gas (argon or helium), to preserve the graphite element and insulation. Typical furnace conditions required for densification were 2200°C for 1 h at 25 MPa.

The density of the hot pressed billets and test specimens was measured using the Archimedes method and He pycnometry (Micromeritics Accupyc 1330). The phases present in the sintered materials were characterized using XRD. After the samples were cross-sectioned and polished to a 1-μm finish, the microstructure of consolidated samples was characterized using optical microscopy and Scanning Electron Microscopy (FEI ESEM 30) with EDX analysis.

Mechanical and thermal property test specimens were prepared with diamond tooling, and ground to a final surface finish in accordance with ASTM C1161 (Chand Kare Technical Associates, Worcester, MA). Vickers hardness was determined using indentations created by a Shimadzu HSV-30. Hardness values were calculated from the average length of the diagonal lines across an indentation made using a load of 49 N applied over a 15 s interval. Hardness indents were made in five groups of 3, starting at the outside edge and working towards the center of a sample, to provide a qualitative evaluation of any radial variation in the material microstructure.

Elastic moduli were measured by the resonance frequency method, using a GrindoSonic on 3 × 4 × 45 mm bars. Two methods were employed to measure flexural strength-bi-axial flexure testing (according to ASTM 1499, using 25.4 mm diameter × 1 mm thick disks) and 4-point bend testing (3 × 4 × 45 mm bars according to ASTM C1161), with a crosshead speed of 0.5 mm/min. Estimates of the reliability of the materials were made and represented by a Weibull modulus that was calculated following ASTM C1239.

Thermal conductivity of the materials was measured in the range –130 to 2000°C (sample size: 1.27 cm dia. × 0.1 cm thick) using the laser flash technique according to ASTM C201. Coefficient of thermal expansion was measured using a pushrod dilatometer in the temperature range of −130 to 1500°C (sample size: 3 × 4 × 10 mm) according to ISO 17562. All thermal property measurements were performed by Netzsch Instruments (Boston, MA).

Finally, arc jet testing was performed on machined flat face models, to evaluate the oxidation/ablation behavior of the HfB_2/SiC material. Fig. 2 shows a schematic of the types of arc heaters in use at Ames Research Center. The arc heater produces a high-temperature gas stream by combined radiative, conductive and convective heat transfer from a high-voltage DC electric arc discharge to a gas flowing through a cooled column. The facilities at Ames are capable of input power levels of 20 to 60 MW for up to 30-min durations. The facilities can also test a variety of sample sizes and shapes, such as 80 × 80 cm 2-dimensional articles for panel and seal applications, or 3-dimensional models. The Ames Arc Jet facility can also test samples up to 60 cm in diameter, for aero surface control/response applications. Examples of various HfB_2 UHTC based models that have recently been tested at Ames are shown in Fig. 3.

A photo of an as-machined flat face arc-jet model is shown in Fig. 4. The model is 25.4 mm in diameter and the overall height is 8 mm. The notch in the base of the model, shown in the lower left hand picture in Fig. 4, is used to pin the model into the holder. Models were placed in SiC-coated graphite holders (shown in the right hand image of the same figure) which enabled test durations in excess of 10 min; an uncoated graphite holder would have allowed only for a few minutes of testing. Models and holders were then attached to a water-cooled arm (sting), as shown in Fig. 5, that moved the models in and out of the plasma stream.

A variety of instrumentation was used to calibrate the arc jet conditions and to measure the thermal response of the materials. The cold wall heat flux values, shown in Table I, were measured using a copper Gardon gage and are referenced to a 76 mm diameter hemisphere. However, the hot wall heat flux values at the model's surface are different from these calibrations, because of differences in model geometry and differences between the catalycity of the models and the catalycity of the copper Gardon gage. Detailed discussion of the heat flux at the surface of the model is beyond the scope of this work. To differentiate the two conditions, for this text, the first will be designated as "low" and the second will be designated as "high" condition.

Two 1-color and one 2-color optical pyrometers were used to make surface temperature measurements during the tests. Based on previous experiments conducted by ManLabs, an emittance of 0.65 was assumed for the 1-color pyrometer [13]. In general there was excellent agreement between the different pyrometers, so

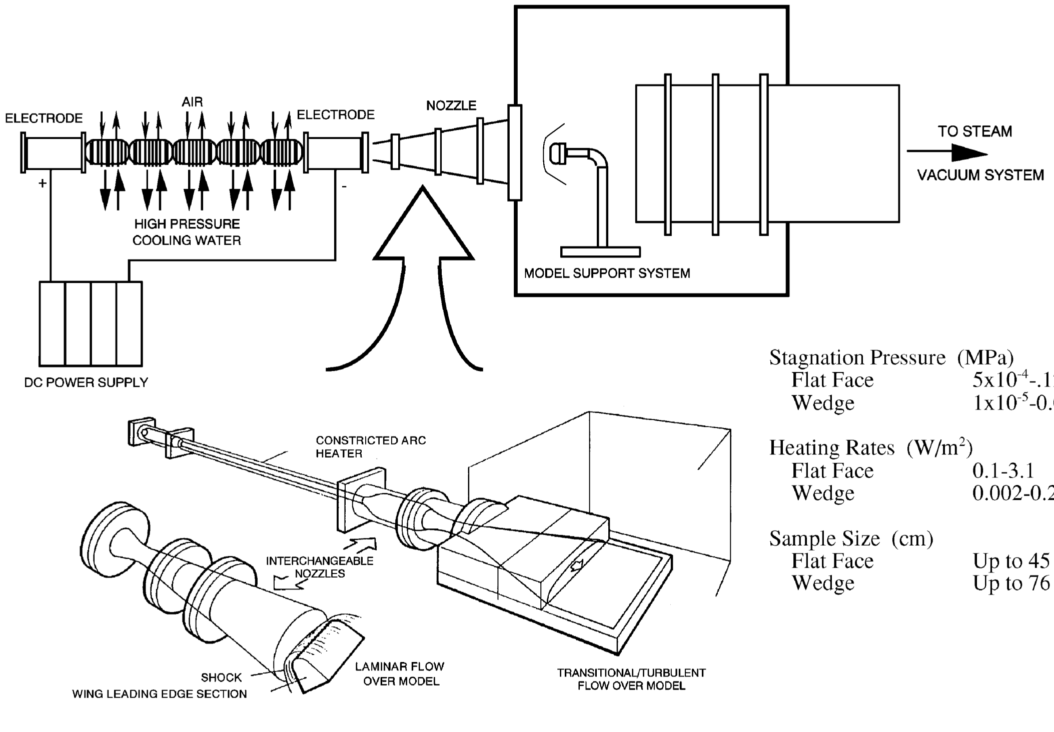

Stagnation Pressure (MPa)	
Flat Face	5×10^{-4}-.12
Wedge	1×10^{-5}-0.015
Heating Rates (W/m^2)	
Flat Face	0.1-3.1
Wedge	0.002-0.2
Sample Size (cm)	
Flat Face	Up to 45
Wedge	Up to 76 x 76

Figure 2 Schematic of the Ames Arc Jet facilities, showing the basic construction of an arc jet. Figure also demonstrates the various nozzle types available for performing testing on 3-dimensional samples or flat panels [13].

Figure 3 The family of arc jet models (flat-face, cone and wedge) fabricated and tested at NASA Ames.

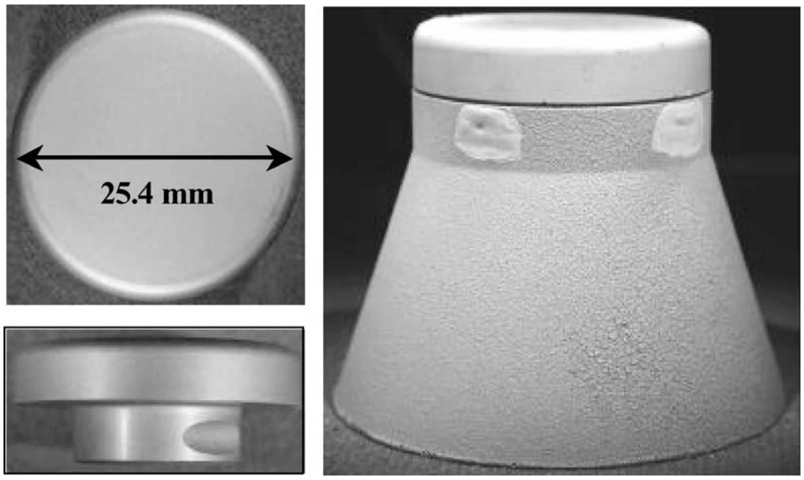

Figure 4 Pre-test photo of a flat face arc jet sample, top, side and in a SiC coated graphite holder. Graphite pins were used to hold the sample in place. To prevent the pins from eroding, the ends were coated with a SiC paste (lighter color spots on the holder).

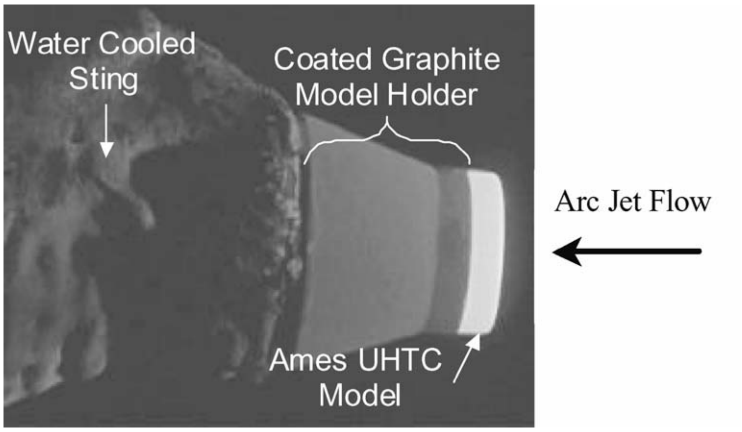

Figure 5 Photo of a flat-face sample during an arc jet run. Sample and holder are shown attached to a water-cooled sting arm, which serves to move the sample in and out of the flow.

data from each pyrometer is not shown in every figure. Instrumentation (such as thermocouples or optical pyrometers, for making in-depth or back face temperature measurements) was placed inside a cavity within the sting arm, for protection during the experiments.

For each condition shown in Table I, a model was tested twice for 10-min for a total run time of 20 min. After each exposure, the models were weighed and optical images of their surfaces were taken. After the first test, the models were re-assembled in a new holder and

TABLE I Summary of arc jet sample characteristics, conditions and measured surface temperatures

Model #	Density (g/cc)	Calibrated heat flux (W/cm^2)[a]	Heat flux as referenced in this text	Pressure (MPa)	Steady state surface temp.[b] (°C)	Duration[c] (s)
FF-61-1	9.59	285	Low condition	0.005	1690	1200
FF-61-2	9.57	350	High condition	0.007	2360	1200

[a] Cold wall heat flux as referenced to a 76 mm dia. Cu hemisphere.

[b] Temperature measured during second exposure.

[c] Consists of two 10 min exposures.

re-instrumented, to enable in-depth or back-face temperature measurements. In this current work we have limited our discussions to the surface temperature measurements only.

3. Results and discussion

3.1. Processing

Table II shows the results of the chemical analysis performed on the raw, milled and hot pressed powders. In the HfB_2 powder, the highest impurities were C, O and Zr. Typically, Hf and Zr are found together in natural ores and Hf is a by-product of Zr refining. As a result of their common chemistry and source, both Hf and Zr tend to retain certain impurity levels of each other [14]. Metal borides are typically made by reaction of the purified metal oxide with boron- and carbon-containing species. This reaction is capable of yielding large quantities of powder, but it may contain by-products, such as borates. Currently, it is unclear what level of contaminant causes a significant effect on the high temperature properties of UHTCs. As shown in Table II, C and O account for the largest quantity of contaminants in the powders used for this work. In the SiC powder, O is the highest impurity. The milled powder mixture shows higher concentrations of W and O than before. This is due to contamination introduced during the milling process, which used tungsten carbide (WC) milling media.

XRD scans of the raw HfB_2 powder, the mixed HfB_2/SiC powder and the as-hot-pressed sample (Fig. 6) clearly show that HfB_2 peaks dominate. In all of the scans it is difficult to discern SiC peaks because of X-ray absorbance by the HfB_2 phase. Present in the scans of the raw and milled powders are small peaks indicating the presence of HfO_2 and some ZrO_2. After hot pressing, some HfC was detectable in the solid sample.

The median particle size of the HfB_2 and SiC in the as-received powders is 4.1 and 1.6 μm respectively (Table III). After milling for 2 h, the median particle size of the HfB_2-20 vol% SiC mixture is 2.1 μm. It is uncertain whether further reduction in particle size would benefit processing or material properties. A milling time of 2 h was chosen simply to minimize contamination from oxygen and milling media. To further minimize contamination, cyclohexane was used as a milling solvent and an inert atmosphere was used to dry the powders. The resulting particle size of the milled HfB_2/SiC powders is also shown in Table III. Some oxidation of the newly formed surfaces was inevitable during processing, and the O content of the milled powders increased to 0.89 weight percent.

As mentioned previously, mixed powders are hot pressed at 2200°C and 25 MPa for 1 h in graphfoil-lined graphite dies. In this work, both 25 mm diameter ×50 mm tall and 50 mm diameter × 50 mm tall cylindrical billets were hot pressed. These billets required about 250 and 1000 g of powder, respectively.

The theoretical density for the HfB_2-20 vol% SiC material is 9.54 g/cm^3 assuming a HfB_2 density of 11.12 g/cm^3 and a SiC density of 3.2 g/cm^3. Fig. 7 shows the densities of thin disks cut along the billet axis as a function of position within the billet, from top to bottom. The disks were 25 or 50 mm in diameter and 1–2 mm thick. Plotted in this figure is bulk density as a function of position, for two 25 mm diameter billets, #52 and #53, and a 50 mm diameter billet, #64. As can be seen for the 25 mm diameter billets, the densities range from about 9.5 to 9.75 g/cm^3 which is ∼2% higher than theoretical. Three possibilities were looked at in trying to explain the variations in density. First, assuming that all of the oxygen contamination of the SiC was in the form SiO_2, calculations indicate that at the measured levels, 0.89 wt%, oxygen in the SiC would

TABLE II Elemental characterization of raw powders, milled powders and hot pressed materials

Sample	Chemical analysis (wt%)								
	B	C	Co	Hf	O	Si	W	Zr	Other
[a]Raw HfB_2	10.49	0.11	–	88.7	0.44	–	–	0.29	0.014
[b]Raw SiC	–	29.8	–	–	0.49	69.7	–	–	0.048
Milled HfB_2/SiC	9.61	2.02	0.04	82.7	0.89	3.59	0.83	0.37	0.006
Hot pressed	9.7	1.81	0.02	83.4	0.03	3.86	0.75	0.40	0.01
Theoretical HfB_2	10.8	–	–	89.2	–	–	–	–	–
Theoretical SiC	–	30.0	–	–	–	70.0	–	–	–
Theoretical HfB_2/SiC mix	10.1	2.0	–	83.2	–	4.7	–	–	–

[a] Raw HfB_2 – Al = 0.014%.

[a] Raw SiC – Al = 0.012%, Fe = 0.014%, Ni = 0.011%, V = 0.011%.

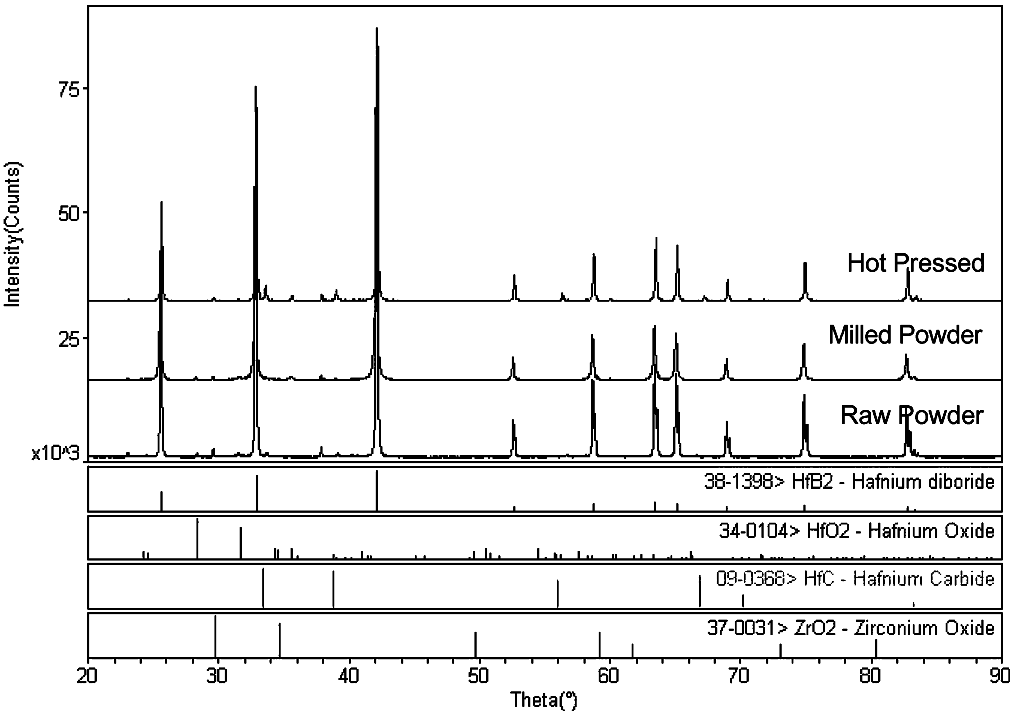

Figure 6 X-ray scans of raw powders, mixed/milled powders and an as-hot-pressed monolithic billet.

affect final composite density less than half a percent. Next, we assumed the 0.83 wt% tungsten was present as tungsten carbide. With that assumption, calculated density increases less than half a percent, which again is not the observed difference. Density measurements using the Archimedes method indicate that there is no open porosity within the billets. Examination of polished cross-sections using SEM also do not indicate the presence of closed porosity within the billets. Instead, image analysis from several SEM micrographs suggests that the higher than theoretical densities are attributable to a slight loss of SiC during hot pressing. Image analysis clearly shows that a loss of 2–3% SiC occurs, and revised volume fractions of SiC correlate well with observed densities. Additional measurements are required, however, to obtain sufficient statistics.

To accommodate the larger diameter and mass of the samples, the hot pressing profile used for the 50 mm diameter billets was modified slightly from that used for the 25 mm diameter billets, by increasing ramp and dwell times. For the single 50 mm billet that was sliced and inspected, Fig. 7 indicates that there is a gradual increase in the density of the larger billet from top to bottom of the sample. This is probably due to sub-optimal processing of the larger billets, because a limited number of these 50 mm billets have been manufactured to date.

TABLE III Particle size analysis for raw starting powders and powders that were attritor milled for 2 h

	Particle size (m)		
Sample	*d*(0.1)	*d*(0.5)	*d*(0.9)
Raw HfB_2	1.2	4.1	18.3
Raw SiC	0.4	1.6	3.9
Milled HfB_2/SiC	0.7	2.1	4.7

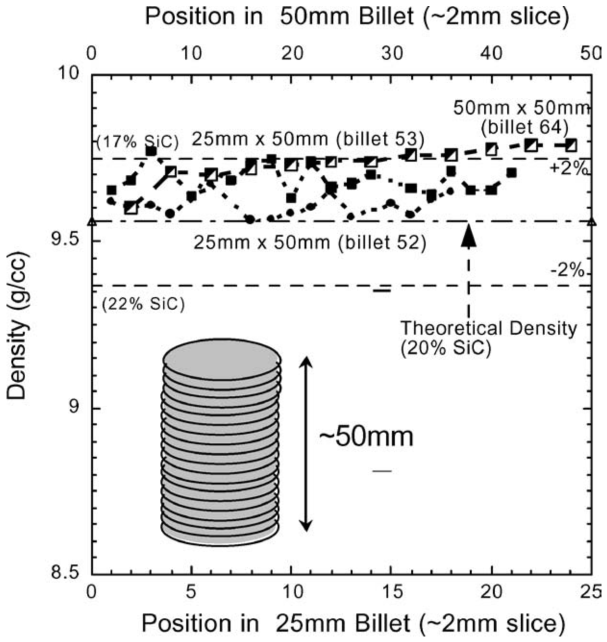

Figure 7 Plot of density vs. position within a billet. There remains a noticeable gradient axially within 50 mm diameter billets that does not appear to exist in 25 mm billets.

Chemical analysis of the raw HfB_2 powder indicates the presence of some C in the raw powder, which may be excess from the carbothermal reduction of HfO_2 to yield HfB_2 (in the presence of B and C). Residual HfO_2 and possible ZrO_2 are also present to some degree in the raw powders and even more so after additional oxygen contamination during milling. Chemical analysis of the hot-pressed material shows the continued presence of W remaining from the milling media. Nevertheless, there is a significant drop in O content, from 0.89% in the milled powders to 0.03% in the hot-pressed material. It is acknowledged that the O contents have been

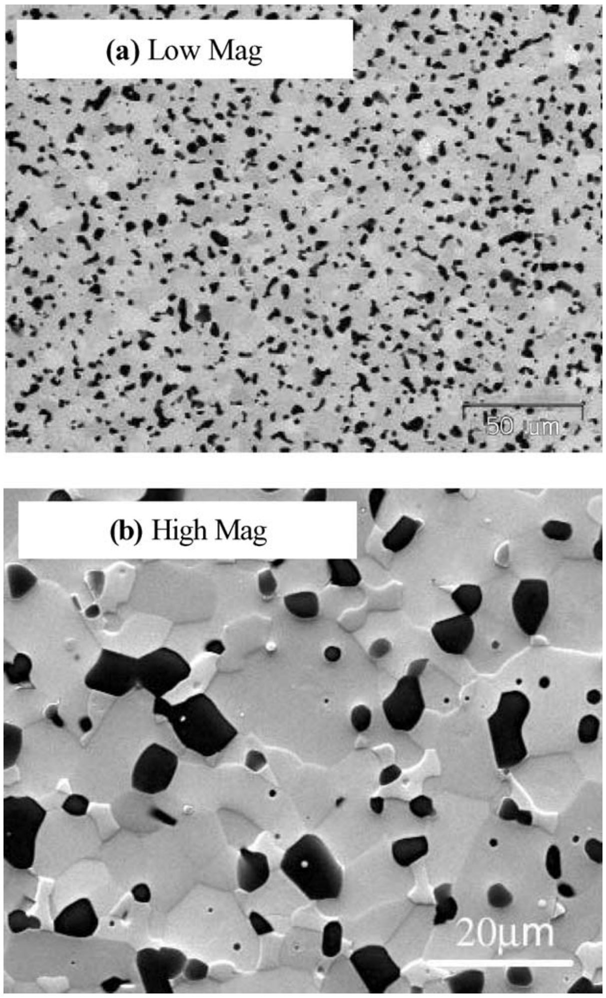

Figure 8 Representative microstructures of a 50 mm × 50 mm billet showing uniform microstructures (low magnification) and grain structure of the SiC phase (black) within the HfB_2 phase (gray), (high magnification).

measured only on a small number of raw and milled powders and hot-pressed billets, so the statistical variation in O content from lot to lot and billet to billet is not known. Nonetheless, from this limited data set, it is believed that the drop in O content observed in the hot-pressed billet is a significant result that occurs during each hot pressing run, and does not represent a statistical anomaly. XRD also indicates the presence of a slight amount of HfC in the final hot pressed material.

The densities of the flat face arc jet models, machined from a single 50 mm diameter billet, were very similar −9.59 and 9.57 g/cc respectively. Fig. 8 shows SEM micrographs of polished cross sections from hot-pressed HfB_2 with a nominal 20% SiC content. The dark phase in the images is SiC and the lighter phase is HfB_2. Fig. 8a is a low magnification image showing the uniform distribution of the SiC phase in the HfB_2 matrix. Fig. 8b is a higher magnification image showing the individual SiC particles and HfB_2 grains. For the most part, SiC grains range from ∼2–10 μm, while the HfB_2 grains are typically 10–20 μm.

TABLE IV Room temperature mechanical properties measured of the most recent Ames-produced 50 mm billets

Billet #	Vickers hardness (GPa)	Modulus (GPa)	Strength (MPa)	K_{IC} (MPa$\sqrt{m}$)
61	17 ± 0.3	536 ± 5	406 ± 57	–
62	18 ± 0.6	547 ± 3	411^a	–
63	17 ± 0.6	546 ± 8	415 ± 81	4.2^a
65	17 ± 0.7	549 ± 8	453 ± 46	4.1 ± 0.2
SHARP-B2	21 ± 1.0	524 ± 45	356 ± 91	–

[a] Only one sample was tested, therefore, standard deviation was not calculated.

3.2. Properties

Vickers hardness values for the materials processed during this work are between 17 and 18 GPa. These numbers are comparable to the values observed in recent materials manufactured for the SHARP-B2 program (19 to 21 GPa), as shown in Table IV. SEM images of the indents (Fig. 9) show that the crack propagation in the two materials is substantially different. In the materials developed at ARC, the cracks tend to propagate through the grains (intra-granularly) whereas cracks in the previous materials tend to propagate between grains (inter-granularly).

The elastic modulus of the Ames materials, ∼540 GPa, is slightly higher than previous material measurements (Table IV). The higher modulus is likely the result of a slight reduction in the SiC content of these materials compared to the SHARP-B2 materials, due to the loss of SiC during hot-pressing, as discussed previously. The room temperature fracture toughness of these materials averages 4.1 MPa$\sqrt{m}$, which is comparable to the toughness observed in other monolithic ceramics.

Average strengths of the Ames materials are greater than 400 MPa, which is again slightly higher than in

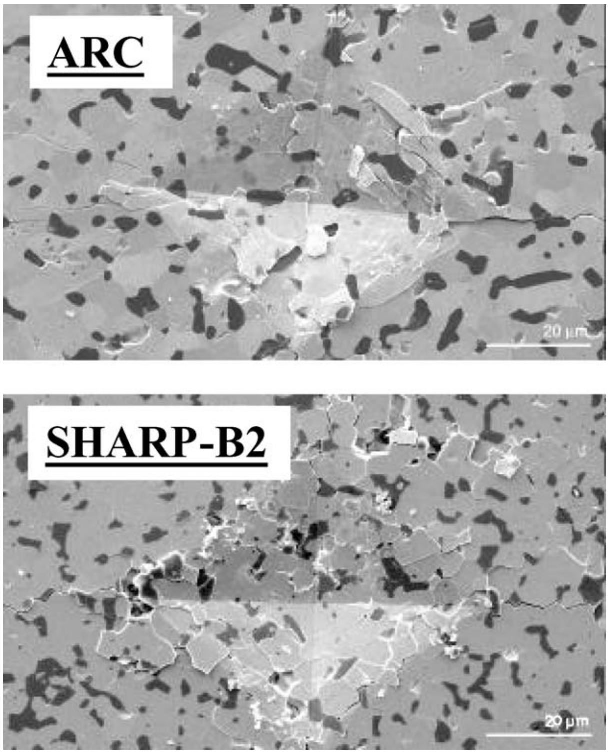

Figure 9 Hardness indents in Ames and SHARP-B2 HfB_2-SiC composites.

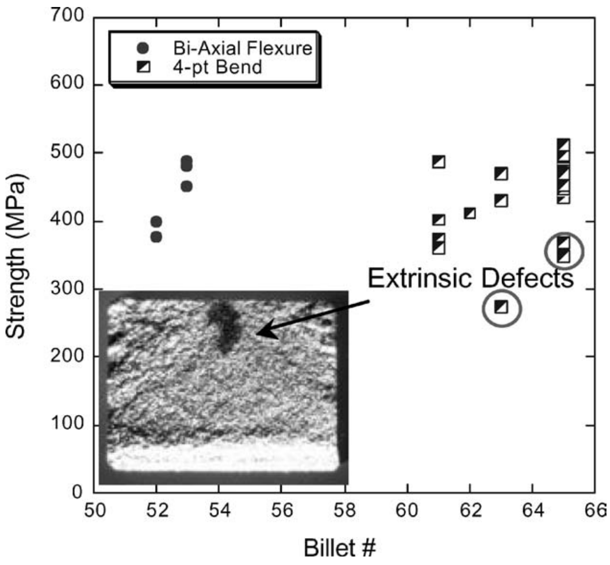

Figure 10 Plot of strength vs. billet number. Circles indicate data points where failure was due to graphite inclusions imparted into the materials during processing. Inset image is of a bend bar fracture surface showing the observed graphite flaws.

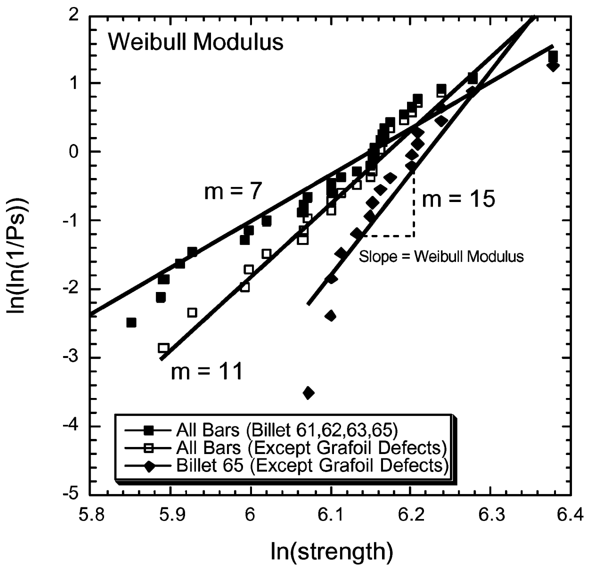

Figure 11 Plot of strength vs. probability of survival (P_S) that yields the modulus of statistical reliability for ceramics or Weibull modulus.

previous materials (Table IV). In general, during this study, the average strengths and strength distributions have improved with processing experience, i.e., with the increased numbers of billets processed. This is most clearly seen in Fig. 10, which plots the strengths of individual test specimens as a function of billet number. As this figure shows, the strengths for billet #65 have a very narrow distribution, except for two outlying specimens with considerably lower strengths. These outliers and the lowest valued strength specimen from billet #63 all showed large C defects on the fracture surfaces (see inset image in Fig. 10). We believe that these C defects are graphfoil flakes that were accidentally introduced into the specimens during the die packing process. If these defects are eliminated from consideration, the strengths and strength distributions for billet #65 appear very promising.

The effect of these large extrinsic graphite defects on the material's strength can be seen in the Weibull plot in Fig. 11. The first line plots materials from billets #61, #62, #63 and #65, all 4-pt bend specimens (billet #64 was not mechanically tested as it was sliced to evaluate axial density gradients). The Weibull modulus for this set of specimens is ∼7. If we take this same data set, but eliminate the bars that failed from the large extrinsic graphfoil defects observed by fractography, the Weibull modulus increases to 11. Going further, if we plot the data from billet #65, without the bend bars that failed from the graphfoil defects, the modulus improves to 15, which is very good for a monolithic ceramic.

The coefficient of thermal expansion (CTE) of the current materials, as a function of temperature, is plotted in Fig. 12. For HfB_2-20 vol% SiC, the CTE increases from $\sim 3.5 \times 10^{-6}$/K at $-100°C$ to $\sim 7 \times 10^{-6}$/K at 1600°C. As expected, the CTE falls between that of pure HfB_2 and pure SiC. The UHTCs relatively large CTE, compared to more traditional thermal protection materials such as silica-based tiles, provides a number of design challenges that must be considered. The large CTE makes the materials less resistant to thermal shock. The large CTE also makes it difficult for designers trying to account for the CTE's of multi-part components, where the goal is to prevent cracking due to part impingement as a result of expansion during heating.

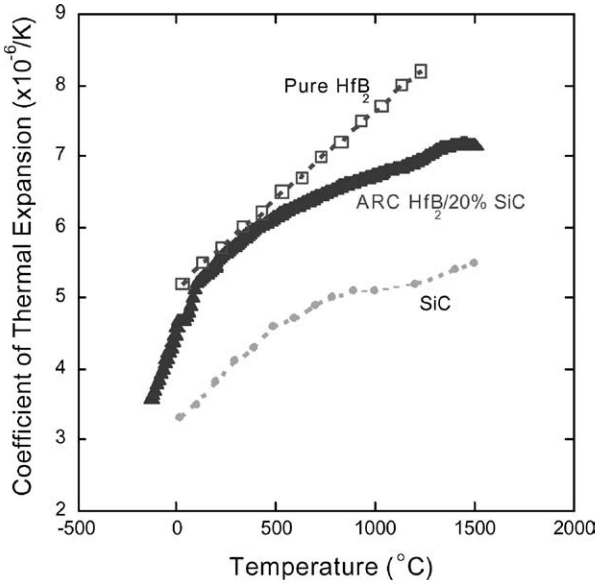

Figure 12 Thermal expansion of ARC HfB_2/SiC in comparison to pure HfB_2 and pure SiC.

Thermal conductivity measurements were performed on materials from 25 and 50 mm diameter billets, to investigate the consistency from billet to billet. Fig. 13 shows the conductivity as a function of temperature from −100 to 2000°C, for both ARC specimens. This figure shows that there is a slight billet-to-billet variation but the trends are the same: a slight increase in conductivity with temperature. However, there is a significant difference in trends between the current ARC materials and materials from previous eras, such as those from ManLabs and the SHARP-B2 program,

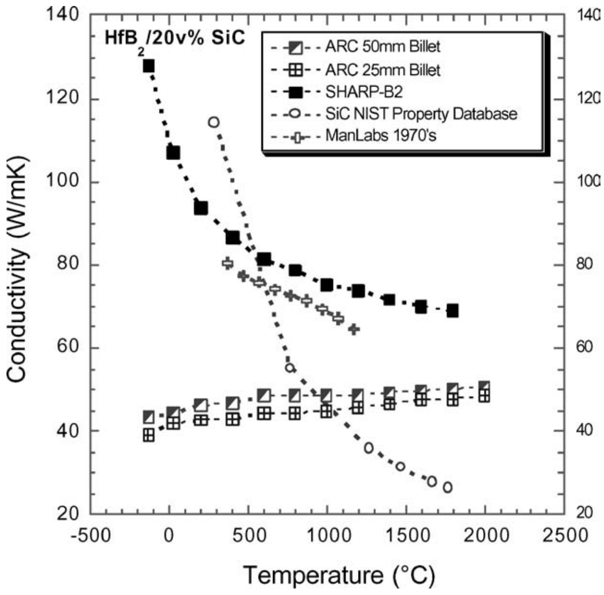

Figure 13 Plot of thermal conductivity for the Ames materials in comparison to previous work on HfB_2 materials [11, 12].

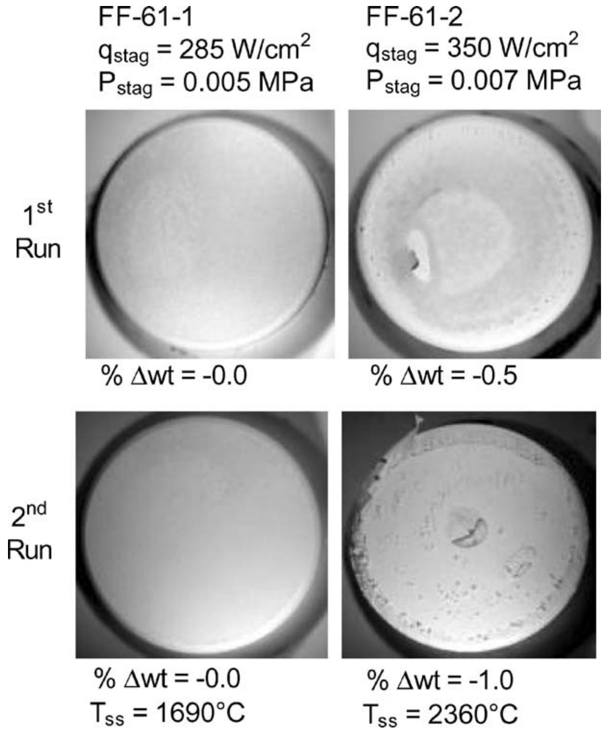

Figure 14 Optical images of flat-face arc jet specimens after their first and second exposures. Each exposure was for 10 min.

which are also shown in the figure. Materials manufactured for the previous works have significantly higher conductivities (>100 W/mK) at room temperature and the conductivities rapidly decrease with increasing temperature. For instance, the conductivity in the SHARP-B2 materials decreases from ∼130 W/mK at room temperature to ∼70 W/mk at 1800°C. In contrast, the materials manufactured at ARC have a room temperature conductivity of ∼40 W/mK and the conductivity increases to ∼50 W/mK at 1800°C. The reason for the difference in conductivities is not currently understood, but work is continuing in this area in hopes of increasing the conductivity of the Ames materials.

3.3. Arc jet testing

Fig. 14 provides a comparison of the surfaces of the two flat face models after each arc jet exposure. At the low condition and after two exposures, there was little change in the visual appearance of the surface, no measurable weight gain was observed, and steady state surface temperatures were 1690–1750°C. At the high condition, there was some evidence of surface oxidation after the first exposure and there was a corresponding weight loss of 0.5%. After the second exposure, surface oxidation is more evident, a total weight loss of 1% was measured, and steady state surface temperatures in excess of 2300°C were measured. After the second exposure at the high condition, spalling of the surface oxide layers was evident. As confirmed by XRD analysis, the oxide surfaces consist of HfO_2. The measured weight loss is primarily due to loss of BO, B_2O_2 and SiO because at these high temperatures and low pressures, B_2O_3 and SiO_2 are not stable and are volatilized [15].

Fig. 15 shows the temperature profiles measured by the 1-color pyrometer from each sample during their first and second run. For sample 61-1 (low condition) the temperature of the surface reached ∼1750°C and remained constant. The surface of the model did not change significantly during the two exposures at these conditions: it had only a dusty white appearance but no significant amount of oxidation. This is not unexpected at temperatures around 1700°C, which are close to the use temperatures for SiC, employed as a coating on reinforced carbon-carbon (RCC), and the specimen is in a regime where SiO_2 is relatively stable.

At the high condition, sample 61-2, model temperatures initially followed the profile for sample 61-1 (low) and then increased steadily after 300 s. The surface temperature histories for model FF-61-2 (high condition) for both arc jet exposures are shown in Fig. 16. This figure shows the temperature measurements for both the 1-color and 2-color optical pyrometers. During the initial exposure, the surface temperature rapidly rose and almost leveled off at ∼1800°C for 300 s. Then the surface temperature began gradually to rise, reaching a maximum temperature between 2200 and 2300°C. During the second exposure, the surface temperature rose rapidly to about the same temperature the model experienced at the end of the first exposure: ∼2300°C. After the first exposure, there was a slight amount of oxidation apparent on the model. During the second exposure, the oxide layer thickened substantially. This observation is consistent, as the surface temperature during the duration of the 2nd run was between 2300 and 2400°C, while it only reached these temperatures at the end of the first exposure. As demonstrated in Fig. 16, the 1-color and the 2-color pyrometers were in close agreement during both exposures of this model.

In general, there do not appear to be significant changes in the morphology of the oxide layers radially across the diameter of the model surfaces. A comparison of the images in Fig. 14 shows that the scale of

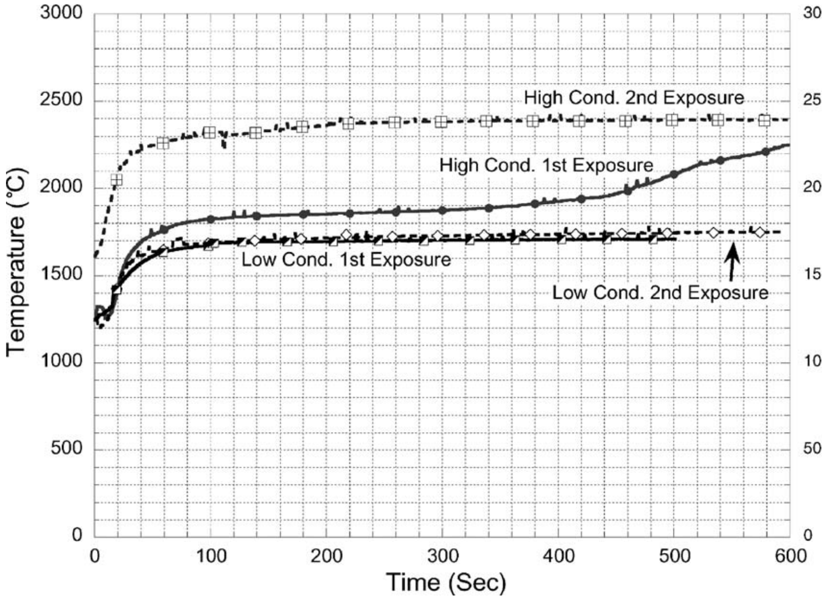

Figure 15 Summary of 1st and 2nd arc jet exposure temperature histories for both high and low condition flat-face samples.

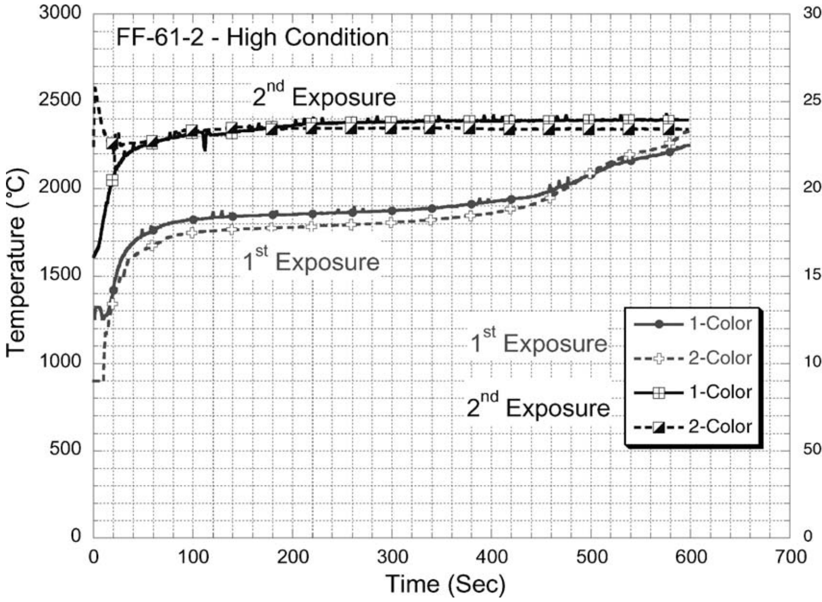

Figure 16 Summary of 1st and 2nd arc jet exposure temperature histories for sample 61-2, high condition. After ∼300 s, the temperature can be seen to rise to levels measured during run 2.

the oxide increases with increasing heat flux from low to high condition. On a microscopic scale, the size of what appear as oxide bumps is significantly larger for sample 61-2 than for sample 61-1 (Fig. 17).

In previous studies by ManLabs, the oxidation of the HfB_2/SiC samples was observed to leave three distinct regions within the material [3]. The first region comprises the surface oxide, primarily composed of porous HfO_2. Below that is a SiC-depleted zone, where the SiC has been oxidized away (active oxidation), leaving behind a porous HfB_2 matrix. Below the depletion zone is the base material.

The flat face models tested in this series were cross-sectioned to determine if a similar structure had formed. Fig. 18 shows an SEM image of a cross section of sample 61-2, tested at the high condition. The image clearly shows a white oxide layer below which there is a SiC depleted region of porous HfB_2 matrix. Similar results were seen on the arc jet model tested at the low condition, sample 61-1, but the SiC depletion layer was considerably smaller. Table V lists the depths of the oxide layers and the depletion layers observed for each of the flat face models.

Oxidation of the SiC clearly plays a significant role in the behavior of these materials during arc jet testing. At 20 volume percent SiC, if the SiC particles

TABLE V Summary of post-arc jet sample characteristics, including SiC depletion and oxide layer thicknesses

Model #	q_{stag} (W/cm^2)	Weight change (%)	Δ Thickness (μm)[a]	Oxide layer (μm)	SiC depletion layer (μm)
FF-61-1	285	0.0	+20	70	2
FF-61-2	350	−1.0	+95	340	740

[a] Refers to the overall thickness increase of the sample.

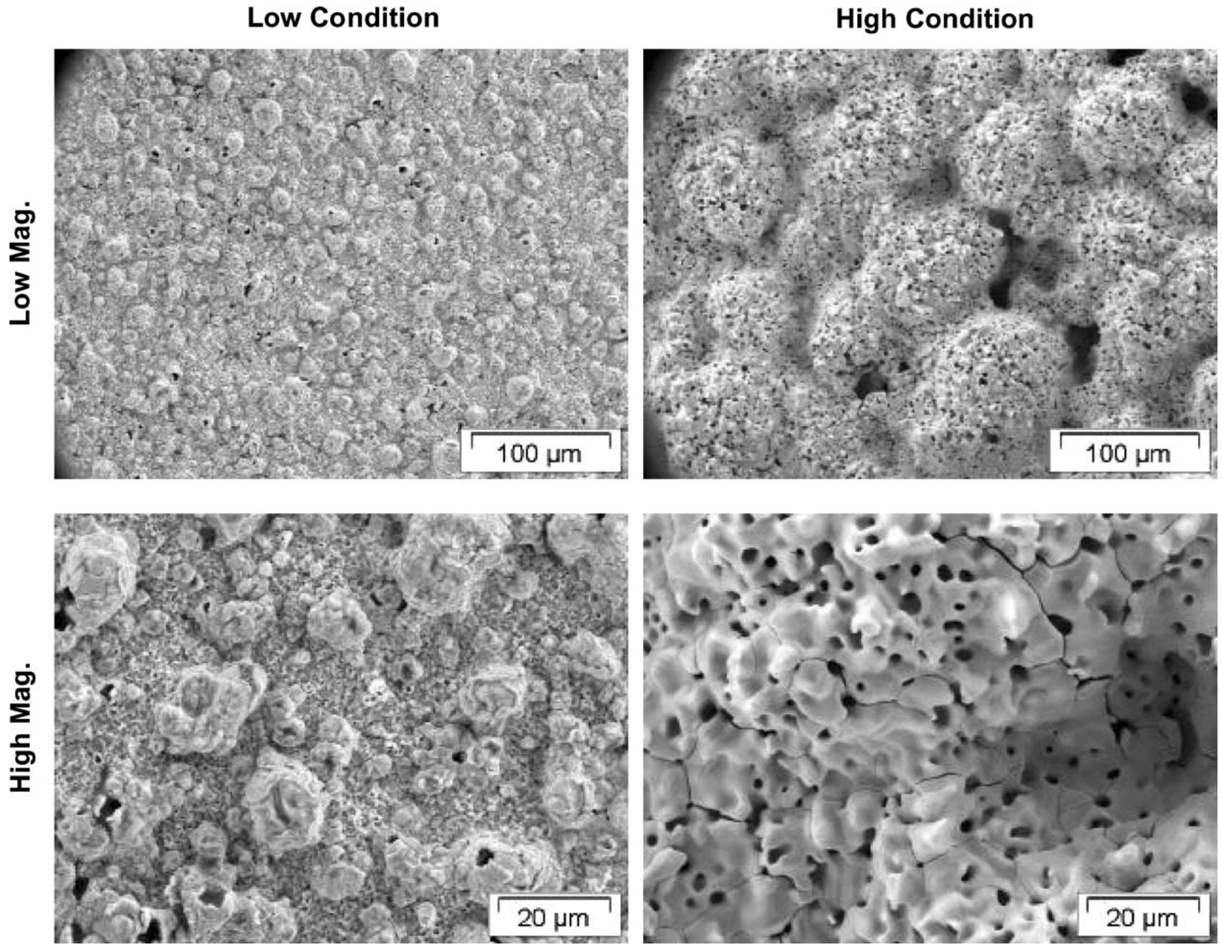

Figure 17 SEM images of the surfaces of FF-61-1 and 61-2 after two 10-min exposures. Images show the bubbly, porous structure of the surface oxide.

are assumed to be small spheres randomly distributed throughout the HfB_2 matrix, the amount of SiC should be above the percolation threshold. This means that the SiC particles form a network that is interconnected in three dimensions. Polished cross sections do not show this interconnectivity, but this is a result of examining a 3-dimensional network in two dimensions. Additional quantitative stereology, including serial sectioning, is needed to verify SiC interconnectivity.

At the low condition, at temperatures approaching 1700°C and at low pressures, the SiC phase forms a passivating layer that helps maintain steady state temperatures. At the high condition, however, the SiC undergoes a transition from passive to active oxidation and the protective SiO_2 layer on the SiC is removed as SiO, CO and CO_2. When the gases SiO, BO and B_2O_2 escape, they pass through the HfO_2, leaving behind channels of porosity. Because HfO_2 is not passivating and does not completely seal the surface of a sample, oxygen can diffuse through the porous oxide channels, and newly exposed SiC surfaces are then subject to further oxidation. Cross sections of the models show that the depth of the SiC depletion layer increases with increasing heat flux. It is hypothesized that the extensive formation of the SiC depletion zone is directly related to the 3D interconnected nature of the SiC phase, allowing continuous oxidization of the SiC during the arc jet tests. During testing, the models were probably in a temperature-pressure regime where active oxidation occurred, drawing more and more SiC out of the sample.

The rise in the temperature during the last 300 seconds of the first exposure of sample 61-2 is probably due to a combination of effects. Initially the UHTC surface is oxidized forming a protective SiO_2 layer. At the high condition however, the SiO_2 layer rapidly becomes unstable and is removed, leading to the formation of a significant HfO_2 layer. The formation of HfO_2 could lead to increased surface catalycity and reduced surface emittance. Since the conductivity of the oxide is lower than that of the diboride, the surface temperature may also increase as oxide thickness grows. As the test continues, BO, B_2O_2 and SiO continue to be evolved. However, the data in Table V suggest that further temperature increase is limited by the continued oxidation of the SiC phase, as identified by the increased depth of the SiC depletion zone at the high condition.

More arc jet testing is required to improve our understanding of the oxidation mechanisms within these materials in high temperature oxidizing environments. Additional testing is also required to verify the reproducibility of the current results. Extended duration testing is needed over a wider range of conditions to provide more kinetic data for these high temperature oxidation reactions. These tests are needed to develop a model to describe, in detail, oxidation of the HfB_2/SiC system. The effect of stagnation pressure on the oxidation rates also needs to be evaluated.

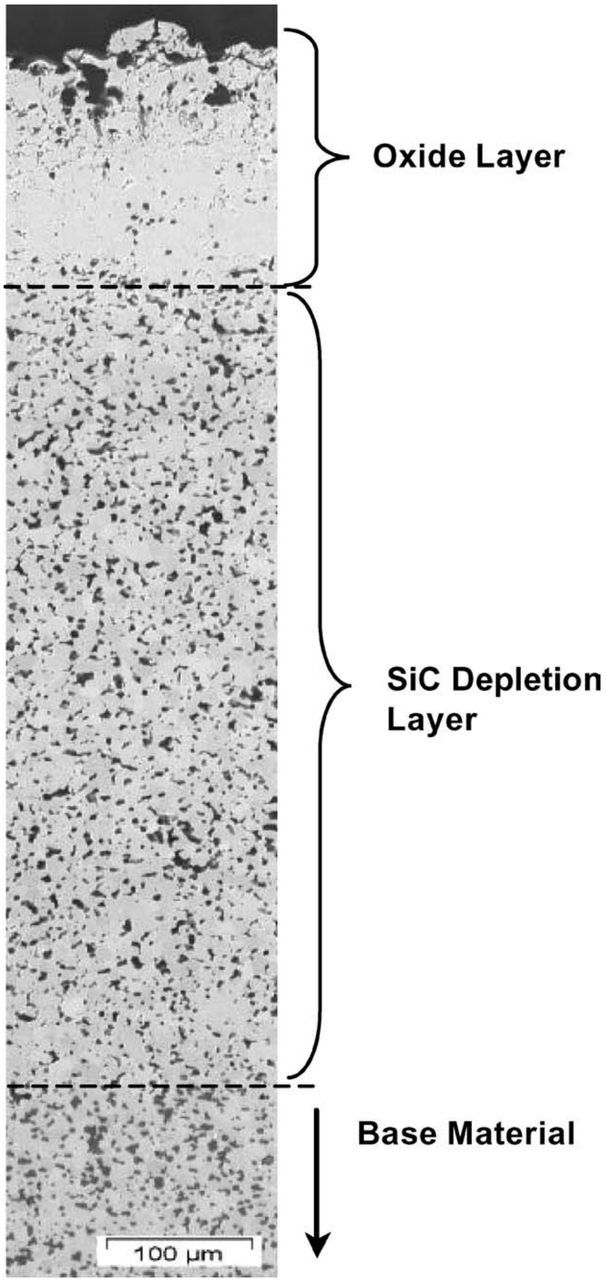

Figure 18 Collage of SEM images of a cross section of flat face model 61-2. Note the bubbly porous structure of the oxide above a porous SiC depleted region. This cross section is the result of two 10-min exposures at the high condition.

4. Conclusion

Dense HfB_2-20 vol%SiC Ultra High Temperature Ceramics (UHTCs) were produced at NASA Ames by hot pressing. The hardness of the Ames materials was similar to, but slightly less than, that which was measured previously (SHARP-B2). The flexural strengths (at room temperature) were greater than those measured in previous studies. Work is ongoing in the evaluation of the high temperature mechanical properties of these systems. Thermal properties of the Ames materials were compared to previous work (SHARP-B2) and the Ames materials had lower conductivities in comparison to heritage results. Work is continuing to understand the cause of the reduced conductivity in the Ames materials.

Arc jet testing of two flat face models provided insight into the oxidation behavior of HfB_2-20 vol% SiC materials. The models were tested at two different heat fluxes, a high and a low condition, for two 10-minute durations each. It was shown that, during the low condition, the passive oxidation of the SiC portion of these materials plays a role in maintaining steady state surface temperatures at around 1700°C. At the higher heat flux, temperature increased significantly and then leveled off, at ∼2400°C, after 300 s. Increased temperatures, at the high condition, were attributed to the presence of a thick porous HfO_2 layer, which changes the surface catalycity, emittance and conductivity. A further increase in temperature is limited by the continued, active oxidation, of SiC. This is evidenced by the presence of a SiC depleted zone, found when performing post-arc jet analysis of the test specimens.

Acknowledgements

The authors would like to thank the following for their contributions in support of this work: the NASA Ames Research Center Arc Jet Crew and Joe Olejniczak, Ed Martinez, Ricardo Olivares, Tom Squire, and Y.K. Chen of NASA Ames Research Center. This work was performed in collaboration with Lockheed Martin under the NASA Space Launch Initiative program. We would like to also thank Paul Sannes, Jerry Draper and Frank Kustas of Lockheed Martin for their support. Portions of this work were also performed under NASA contract NAS2-99092 to ELORET. We would like to thank Jerry Ridge and Mairead Stackpoole of ELORET for their support.

References

1. L. KAUFMAN and E. V. CLOUGHERTY, "Investigation of Boride Compounds for High Temperature Applications," RTD-TRD-N69-73497, Part XXXVII, ManLabs Inc., Cambridge, MA, Dec. 1963.
2. *Idem.*, "Investigation of Boride Compounds for Very High Temperature Applications," RTD-TRD-N63-4096, Part III, ManLabs Inc., Cambridge, MA, March 1966.
3. E. V. CLOUGHERTY, D. KALISH and E. T. PETERS, "Research and Development of Refractory Oxidaton Resistant Diborides," AFML-TR-68-190 (1968).
4. A. K. KURIAKOSE and J. L. MARGRAVE, *J. Electrochem. Soc.* (1964) 827.
5. J. B. BERKOWITZ-MATTUCK, *ibid.* **113** (1966) 908.
6. L. KAUFMAN, E. V. CLOUGHERTY and J. B. BERKOWITZ-MATTUCK, *Trans. TMS-AIME* **239** (1967) 458.
7. E. V. CLOUGHERTY, R. L. POBER and L. KAUFMAN, *ibid.* **242** (1968) 1077.
8. M. M. OPEKA, I. G. TALMY, E. J. WUCHINA, J. A. ZAYKOSKI and S. J. CAUSEY, *J. Europ. Ceram. Soc.* **19** (1999) 2405.
9. S. LEVINE, E. OPILA, M. HALBIG, J. KISER, M. SINGH and J. SALEM, *ibid.* **22** (2002) 2757.
10. F. MONTEVERDE, A. BELLOSI and S. GUICCIARDI, *ibid.* **22** (2002) 279.
11. D. M. SMITH, E. J. FELDERMAN, F. L. SHOPE and J. A. BALBONI, "Arc Heated Facilities," Advanced Hypersonic Test Facilities , edited by F. Lu and D. Marren (AIAA Progress Series (2002) Vol. 198.
12. P. KOLODZIEJ, J. SALUTE and D. L. KEESE, "First Flight Demonstration of a Sharp Ultra-High Temperature Ceramic Nosetip," NASA TM-112215, Dec. 1997.

13. R. PERKINS, L. KAUFMAN and H. NESOR, "Stability Characterization of Refractory Materials Under High Velocity Atmospheric Flight Conditions," Part III, Vol II, ManLabs Inc., Cambridge, MA, 1969.
14. J. B. HEDRICK, "Zirconium and Hafnium," U.S. Geological Survey Minerals Yearbook (1999) p. 86.2.
15. R. H. LAMOREAUX, D. L. HILDENBRAND and L. BREWER, *J. Phys. Chem. Ref. Data* **16** (1987) 419.

Received 5 November 2003
and accepted 23 April 2004